

# In-situ fabrication of metal oxide nanocaps based on biphasic reactions with surface nanodroplets

Zixiang Wei,<sup>\*,†</sup> Tulsı Satyavir Dabodiya,<sup>†,‡</sup> Jian Chen,<sup>¶</sup> Qiuyun Lu,<sup>†</sup> Jiasheng Qian,<sup>†</sup> Jia Meng,<sup>†</sup> Hongbo Zeng,<sup>†</sup> Hui Qian,<sup>¶</sup> and Xuehua Zhang<sup>†,§</sup>

<sup>†</sup>*Department of Chemical and Materials Engineering, University of Alberta, Alberta T6G 1H9, Canada*

<sup>‡</sup>*Centre for Nanoscience and Technology, Madanjeet School of Green Energy Technologies, Pondicherry University (A Central University), Dr. R. Vankataraman Nagar, Kalapet, Puducherry 605014, India*

<sup>¶</sup>*Nanotechnology Research Center, National Research Council Canada, Edmonton, AB T6G 2M9, Canada*

<sup>§</sup>*Physics of Fluids Group, Max Planck Center Twente for Complex Fluid Dynamics, JM Burgers Center for Fluid Dynamics, Mesa+, Department of Science and Technology, University of Twente, Enschede 7522 NB, The Netherlands*

E-mail: zwei3@ualberta.ca

## Abstract

Surface-bound nanomaterials are widely used in clean energy techniques from lithium batteries, solar-driven evaporation in desalination to hydrogen production by photocatalytic electrolysis. Reactive surface nanodroplets may potentially streamline the process of fabrication of a range of surface-bound nanomaterials invoking biphasic reactions at interfaces. In this work, we demonstrate the feasibility of reactive surface nanodroplets for in-situ synthesis and anchoring of nanocaps of metal oxides with tailored porous structures. Spatial arrangement and surface coverage of nanocaps are

predetermined during the formation of reactive nanodroplets, while the crystalline structures of metal oxides can be controlled by thermal treatment of organometallic nanodroplets produced from the biphasic reactions. Notably, tuning the ratio of reactive and nonreactive components in surface nanodroplets enables formation of porous nanocaps that can double photocatalytic efficiency in degradation of organic contaminants in water, compared to smooth nanocaps. In total, we demonstrate in-situ fabrication of four types of metal oxides in the shape of nanocaps. Our work shows that reactive surface nanodroplets may open a door to a general, fast and tuneable route for preparing surface-bound metal oxides. This fabrication approach may help develop new nanomaterials needed for photocatalytic reactions, wastewater treatment, optical focusing, solar energy conversion and other clean energy techniques.

## Introduction

Surface-bound nanomaterials are key components in many clean energy techniques from lithium batteries, solar absorber,<sup>1</sup> solar-driven interfacial evaporation in desalination,<sup>2-4</sup> photocatalytic reactions,<sup>5-7</sup> to wastewater treatment and environment remediation by photolysis.<sup>7,8</sup> Maximizing the performance and functionalities of the materials requires control of spatial distribution and coverage of nanomaterials deposited on a supporting substrate. Exploration of small reactive droplets on surfaces represents a novel strategy for fabrication of surface-bound nanomaterials. Reactions with droplets on surfaces potentially streamline the process of synthesis and immobilization of surface-bound nanomaterials to obtain desired spatial arrangement, surface coverage and materials nanostructures. Recent research has demonstrated the high reactivity of small droplets with possible 1-million time enhancement in reaction rates, compared to the bulk counterpart.<sup>9</sup> However, it remains to be explored how to mediate the reactions between droplets and the bulk surrounding and to establish simple and effective routes for the fabrication of surface-bound nanomaterials.

Small-sized droplets allow the reactant to be compartmentalized at high concentration

and fast mass transfer rate from the surrounding phase.<sup>9-11</sup> The asymmetric local environment on the droplet surface provides active sites for chemical reaction,<sup>9,12</sup> or nucleation and growth of new phases.<sup>13,14</sup> Compared to current techniques developed for selective deposition of metal oxide nanomaterials including direct growth, chemical bonding, electrostatic adherence, or seeding on selectively activated areas,<sup>15-18</sup> droplet reactions are especially effective for material synthesis from chemical reactions between reactants dissolved in immiscible organic and inorganic phases.<sup>9</sup>

Droplet-based synthesis approaches are endorsed by controlled formation of surface nanodroplets that are liquid droplets on a solid surface in contact with an immiscible surrounding liquid.<sup>12,13,19,20</sup> Here *nano* refers to the height of these droplets that range from tens to few hundreds nanometers. Specifically, solvent exchange is the fast and straightforward solution-based process for forming surface nanodroplets.<sup>19,21</sup> Without complex dynamics in evaporating droplets,<sup>22-24</sup> the formation of surface nanodroplets can be tuned by the solution, flow and surface conditions.<sup>19,21,25</sup> Solvent exchange is flexible for the types of substrates, applicable for droplet formation on planar substrates with or without micropatterns, microfibers and even curved wall of microcapillary tubes.<sup>25-27</sup>

Complementary to those droplets flowing in microfluidic channels, surface nanodroplets are stabilized by the substrate. Hence a reactant solution in a flow can be introduced to react with nanodroplets without leading to the uncontrolled collision, coalescence or Ostwald ripening. Reactions between nanodroplets and the reactants in the flow can be leveraged to synthesize surface-bound materials through sequential reactions. As a demonstration, silver nanoparticles were synthesized on droplet surface for fast extraction and sensitive chemical detection.<sup>28</sup>

Up to now, limited studies are available on surface nanodroplets for the synthesis of surface-bound metal oxide. As a common and low-cost photocatalyst with various potential polymorphic characteristics,  $\alpha - Fe_2O_3$  has been widely used in photocatalytic reactions,<sup>29</sup> with advantages in narrow band-gap and high efficiency of absorption up to 40% of the solar

spectrum in the visible range.<sup>30,31</sup> In established protocols, iron oxide-based nanomaterials can be adjusted by varying bottom-up synthesis approaches such as hydrothermal, solvothermal, co-precipitation and many others.<sup>32-35</sup> Iron salt of organic acid, especially iron oleate, is prominently used as precursors in synthesizing nanocrystalline iron oxide-based nanoparticles.<sup>36-38</sup> The external conditions, such as temperature, pressure and among others, are responsible for the secondary noncrystalline phase during the thermal decomposition.<sup>35,39</sup>

In this work, we will take iron oxide as a typical example to demonstrate a simple approach for the in-situ fabrication of surface-bound nanocaps of a range of metal oxides. By our method, oleic acid nanodroplets with desired number density and location are preformed over a solid substrate inside a flow chamber. A flow of iron salt solution is introduced to react with nanodroplets and produce nanocaps of certain spatial arrangement and surface coverage. Moreover, we will show that the composition of nanodroplets can be varied to mediate the nanostructures of the caps and create nanopores along the cap surface. Beyond iron oxide nanocaps, our approach can also be applied to the synthesis of other metal oxides including copper oxide, zinc oxide and yttrium oxide. Our work demonstrates the feasibility of reactive surface nanodroplets as a novel route for in-situ synthesis of surface-bound metal oxides. The prepared nanocaps may be optimized for photodegradation of organic materials in water as demonstrated in this work, and also for optical focusing, plasmonic resonance and among other applications.

## **Experimental section**

### **Chemicals and materials**

Ethanol (90 %), octadecyl trichlorosilane (OTS, 98.9 %), oleic acid (90 %), 1-octanol (95 %) and decane (99 %) were purchased from Fisher Scientific (Canada). While iron (III) chloride (97 %), copper acetate (98 %), yttrium acetate (99 %) and zinc oxide (98 %) was purchased from Sigma-Aldrich (Canada). Water was obtained from a Milli-Q water purification system

(MA, USA). OTS-coated cover glass (Fisher scientific) and silicon wafer (University wafer, USA) were used as the substrate. The coating of OTS was prepared by following the protocol reported in the literature.<sup>40</sup>

## Preparation of metal oxide nanocaps on a substrate

Nanodroplets of oleic acid were produced on a substrate placed in a narrow fluid chamber. The detailed procedure of solvent exchange, as shown in Figure 1a, has been introduced in earlier work.<sup>12</sup> The fabrication methodology of these surface nanocaps is sketched in Figure 1a and b. In the beginning, a ternary solution (Solution A) with volume ratio as ethanol: water: oleic acid (70:30:3.5) filled the chamber. Oleic acid droplets formed on the OTS-coated surface after injecting water (solution B) at a flow rate of 20 ml/hr in step 1. Subsequently, in step 2, Solution C of 0.04 M iron chloride aqueous solution flowed into the fluid chamber at 15 ml/hr.

The droplets of oleic acid react with the iron cation in the flow, forming iron oleate and the complexes droplets over the substrate, as shown in Figure 1b. The reaction for the formation of iron oleate is shown in Eq.1. Finally, in step 3, water at a flow rate of 40 ml/hr flowed into the chamber for 5 minutes to remove excessive unreacted precursors. The substrate was taken out from the fluid chamber after the reaction and then annealed in an oven at different temperatures and environmental conditions as listed in Table 1.



The preparation process for copper oxide, yttrium oxide and zinc oxide is similar to that of iron oxide nanocaps. The only difference is that solution C (precursor solution) changes to 0.04 M copper acetate, 0.04M yttrium acetate or 0.04M zinc acetate, respectively.

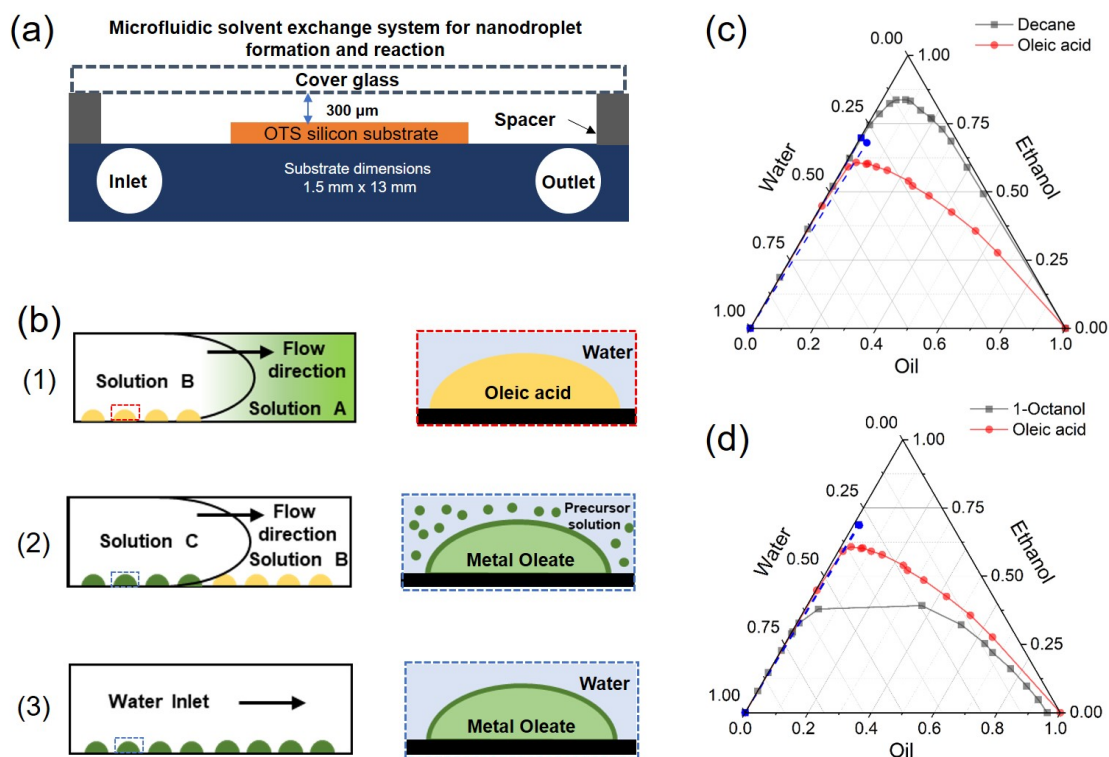


**Figure 1.** A brief sketch of the fluid chamber (a) and surface nanodroplet formation and reaction in the fabrication of nanocaps of iron oleate (b). Solution A: ternary solution of ethanol, water and oleic acid. Solution B: water. Solution C: precursor solution. (c) and (d) are ternary phase diagrams of ethanol, water and oil mixtures. Here, the red lines represent oleic acid. While gray lines represent decane (a) and 1-octanol (b), respectively. The blue lines represent the dilution line during the solvent exchange process. Ternary diagram of oleic acid is reproduced from [Li et al. *J. Phys. Chem. C*. 125, 28, 2021, 15324–15334.]. Copyright [2021] American Chemical Society. Ternary diagram of 1-Octanol is reproduced from [Arce et al. *J. Chem. Eng. Data*. 39 (2), 1994, 378-380.]. Copyright [1994] American Chemical Society. Ternary diagram of decane is reproduced from the IUPAC-NIST solubility database.

## **Preparation of porous iron oxide nanocaps from binary droplets**

For the preparation of the porous iron oxide nanocaps, 1-octanol and decane were used as the secondary oil phase, respectively. The ratio of water, ethanol and oil in solution A is the same as above. However, the oil phase here is a mixture of oleic acid and another oil. In the mixture of oleic acid and the secondary oil, the volume ratio is 2:1.5 for oleic acid and octanol and 2.2:0.3 for the oleic acid and decane. The ternary phase diagram of three oils is shown in Figure 1c and d. The ratio of the oils in surface droplets after the solvent exchange is based on the integrated area between the dilution path and the binodal curve in the Ouzo region, as explained in previous work.<sup>21</sup>

## **Characterization of size and structures of metal oxide nanocaps**

Optical images were obtained using an upright optical microscope (NIKON H6001) coupled with a 10X and 100X lens. A scanning electron microscope (SEM, HITACHI S4800) and atomic force microscope (AFM, Bruker) were used to characterize the surface morphology of the samples. The cross-section of the samples was characterized by a helium ion microscope (Zeiss Orion NanoFAB with Ga FIB). X-ray photoelectron spectroscopy (XPS, Kratos AXIS Ultra) was used to analyze the element and the crystalline state of the samples. The peaks in XPS spectra were analyzed by OriginLab. The TEM characterization was performed by using Hitachi H-9500 Environmental Transmission Electron Microscope (ETEM). An accelerating voltage of 300 kV was applied for the characterization. The selected area electron beam diffraction (SAED) technique was employed for phase identification. The simulation of the SAED pattern was carried out by using Desktop Microscopist (DM). The simulation of high resolution TEM image was then performed by using MacTempasX (Total Resolution).

The nanocaps were prepared on a SiN window (Norcada, Canada) for the imaging of TEM. The dimension of the SiN was 0.05 mm  $\times$  0.05 mm. The SiN window was directly used as the substrate in our fluid chamber, where the surface nanodroplets of oleic acid surface nanodroplets were formed and then reacted with the iron precursor. Iron oleate droplets on

the SiN window were heated in air at 500 ° for 2 hr, respectively. After the samples were cooled down to room temperature, the samples were put into a TEM chamber.

The cross-section images of iron oxide nanocap that was heated at 500°C in air for 2 hr were obtained by FIB-HIM (Zeiss Orion NanoFAB with Ga FIB). A high-energy beam of Ga ion that is perpendicular to the substrate was used to mill the nanocap. Half of the nanocap was milled and from the top view, semicircular of the naoncap remains on the substrate. Then the cross-section of the nanocap appears after the milling by FIB. In order to obtain the thickness of the nanocap, the stage was tilted by 57° from the top view, leading to an elliptical view of the spherical shape. The sketch of the FIB process is shown in Supporting Information SI-1.

**Table 1.** Experimental conditions for fabricating of metal oxide nanocaps.

Metal	Precursor	Heating temperature (°C)	Heating time (hr)	Treatment mark
Iron	$FeCl_3$	75	0.5	I
		300	0.5	II
			2	III
		500	0.5	IV
			2	V
Copper	$Cu(CH_3COO)_2$	300	2	NA
Yttrium	$Y(CH_3COO)_3$	500	2	NA
Zinc	$Zn(CH_3COO)_2$	500	2	NA

## Photodegradation catalyzed by iron oxide nanocaps

Photodegradation of model compounds methyl orange (MO) was performed in a flow chamber, similar to our chamber for performing solvent exchange process. The chemical structure of the model compounds and the degradation path are shown in Supporting information SI-2. Glass substrate decorated with iron oxide nanocaps was used as the top plate. The channel height of the fluid chamber was kept at 150  $\mu m$ . The solution of MO (5 mg/l) was continuously injected into the chamber, controlled by a syringe pump at a constant flow rate of 1 ml/hr. It took 45 minutes for injected MO solution to pass the fluid chamber. The fluid

chamber was exposed to  $21.6 \text{ W/m}^2$  intensity of the simulated solar light. The exposure time of the solution was also 45 minutes. The treated solution was collected and characterized by a UV-vis spectrometer (Varian Cary 50). The efficiency of the photodegradation is defined as:

$$E = \frac{(Abs_{before}) - (Abs_{after})}{Abs_{before}} \quad (2)$$

Where, E is the efficiency of degradation.  $Abs_{before}$  and  $Abs_{after}$  are the UV absorbance of MO solution at the peak of 464 nm before and after the photodegradation, respectively.

In order to evaluate the efficacy of the different nanocaps, we normalized the efficiency by the surface coverage of nanocaps:

$$E_n = \frac{(E_{cap}) - (E_{glass})}{S} \quad (3)$$

Here,  $E_{cap}$  refers to the degradation efficiency by using the nanocaps-decorated top plate. While  $E_{glass}$  refers to the degradation efficiency by using bare glass as the top plate. S is the surface coverage of the nanocaps.

## Results and discussion

### Formation and morphology of iron oxide nanocaps

Surface nanodroplets of oleic acid were produced by using the solvent exchange process. The droplet size was controlled from a few to tens of  $\mu\text{m}$  in lateral radius ( $R$ ). The flow of iron chloride aqueous solution was injected into the chamber to react with surface nanodroplets. Droplets change the shape during reaction with iron cation as shown in Figure 2a. Initially, at  $t=0$  s just after the injection of iron chloride solution, oleic droplets have no significant change. Further proceedings of the reaction at  $t=14$ s, a boundary rim was developed around the bigger surface droplets and some small droplets were formed on the space area. Splitting of the reactive droplets may be due to interfacial tension stress induced by heterogeneous

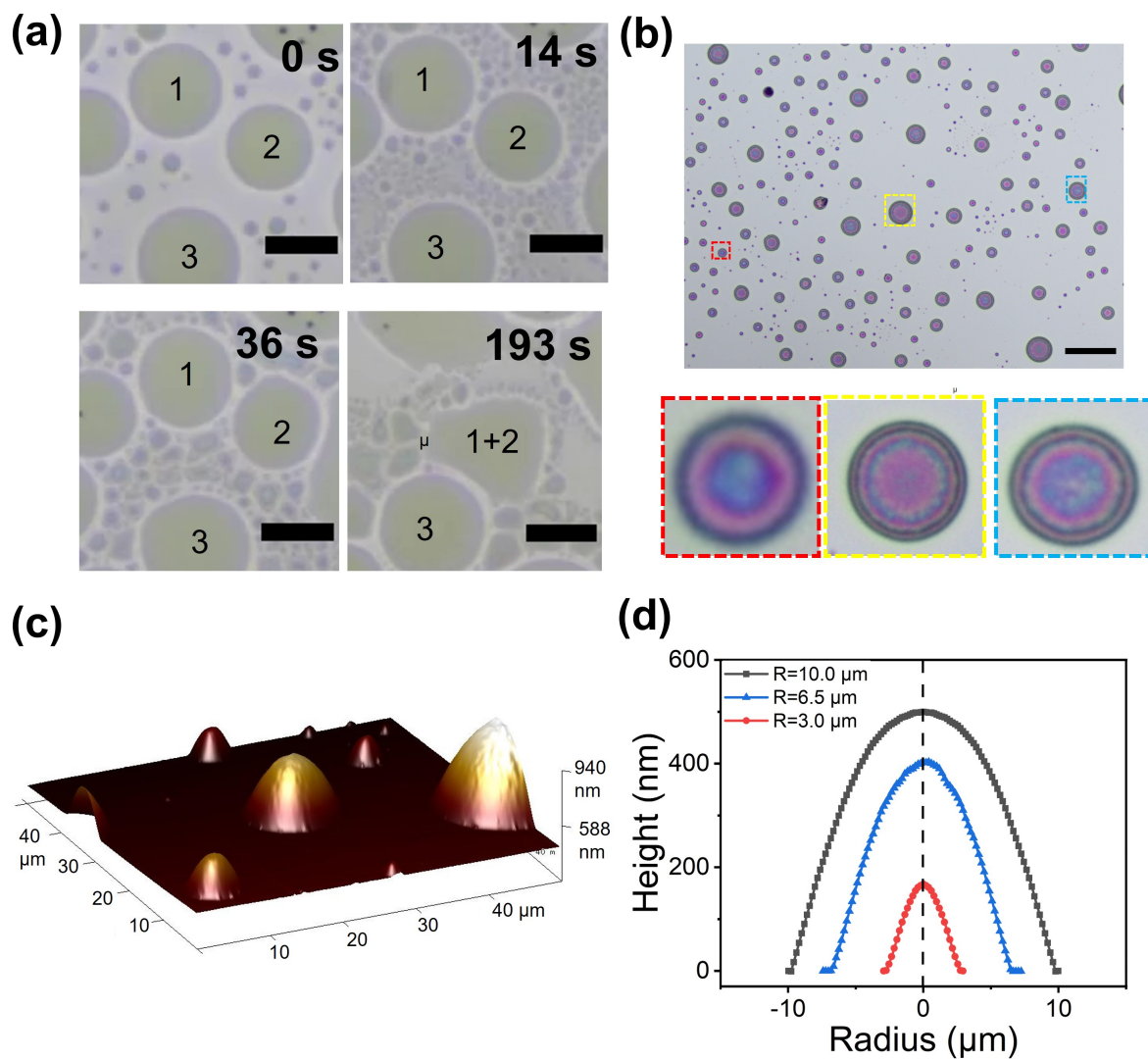


**Figure 2.** (a) Optical images of surface nanodroplets during the reaction at 0 s, 14 s, 36 s and 193 s. (b) Iron oxide nanocaps on the substrate. (c) Morphology of the nanocaps obtained by AFM after heating at 500°C for 2 hours in air. (d) The height profiles of the nanocaps from AFM reveal that the contact angle of the nanocaps around 7°. Length of scale bare: 20  $\mu m$  in (a) and 50  $\mu m$  in (b).

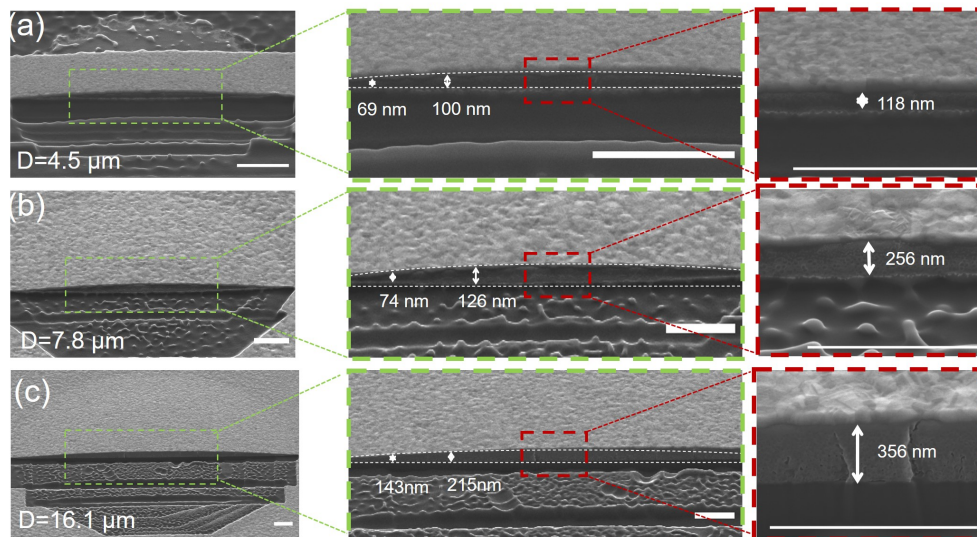


**Figure 3.** Images of three nanocaps milled by focused ion beam at diameter of (a)  $4.5 \mu\text{m}$ , (b)  $7.8 \mu\text{m}$  and (c)  $16.1 \mu\text{m}$ . The images on the left were taken at  $57^\circ$  from the normal plan to the substrate. Length of the scale bar:  $1 \mu\text{m}$ .

distribution of chemical species on the droplet surface.<sup>41</sup> After a specific time interval, the tiny droplets expanded and merged into larger droplets. Finally, at 193 s, some adjacent droplets merged while other droplets still remained as individuals, but all droplets assume spherical cap shape eventually.

At the completion of the droplet reaction, the substrate with iron oleate droplets was taken out from the chamber and heated at elevated temperatures. The final products appear to be semitransparent with colorful Newton rings clearly visible in optical images, as shown in Figure 2b. The semitransparent suggests the ultra-thin structure of the product after heating. Cross-sectional profiles of three structures were obtained from the AFM images in Figure 2c and d. These structures have the shape of spherical caps with an apex less than  $1 \mu\text{m}$  even for the exceptionally large one. The height of the structure in Figure 2 ranges from 164 to 500 nm and the lateral diameter from  $5.4$  to  $19.6 \mu\text{m}$ , with a contact angle around  $7^\circ$ . Following the naming convention of surface nanodroplets, we refer to these structures as nanocaps.

The surface coverage of oleic acid droplets was 40% before the reaction and decreased to

11% after heating. The shrinkage at elevated temperature is due to decomposition of iron oleate ( $Fe(C_{18}H_{33}O_2)_3$ ) to iron oxide ( $Fe_2O_3$ ). The mass loss from thermal decomposition is around 91% based on simple elemental analysis. The size distribution of surface droplets also changed after the heating process, as shown in SI-3. The surface nanodroplets are dominated at the diameter of 1 to 2  $\mu m$ . The nanocaps are most at the diameter of 3 to 4  $\mu m$  with a thickness of 180 to 270 nm. When the surface oleic acid reacts with the iron precursor, the droplets are expanded, as shown in Figure 2a. Some small droplets merge together to form a larger droplet. While other small droplets disappear during the heating due to the shrinkage. This phenomenon is why the most probable size of the nanocaps is larger than that of oleic acid droplets.

The surface coverage of nanocaps can be varied by conditions from formation of surface nanodroplets. Larger surface nanodroplets with a large interval of each other formed larger nanocaps with low surface coverage after reaction and heating, as shown in SI-4.

The inner structure of the nanocap was analyzed by using FIB that can mill half of the nanostructures. The cross-section of the nanocap is exposed along the central line. As shown in Figure 3, the nanocaps of all sizes have a homogeneous filled inner structure. Such internal structure indicates that the reaction was not limited to the droplet surface. Oleic acid inside the droplet was also converted to oleate by reacting with an iron precursor in the solution.

The morphology of the nanocap suggests that the reaction between iron precursors and oleic acid droplets is not only happened at the interface but within the whole droplet. Specifically, the carboxyl group of oleic acid reacts with the iron cation at the droplet surface, which results in the formation of iron oleate,  $Fe(C_{18}H_{33}O_2)_3$ . During the reaction process, the -OH group of the oleic acid was replaced by O-Fe. The formed iron oleate may diffuse inside of the droplet. The fresh oleic acid molecules move to the interface, leading to a continuous reaction. The reaction occurs from the water-oil interface and then extends to the whole droplet within a few minutes when the droplets stopped deformation.

## Effect of time and temperature of heating

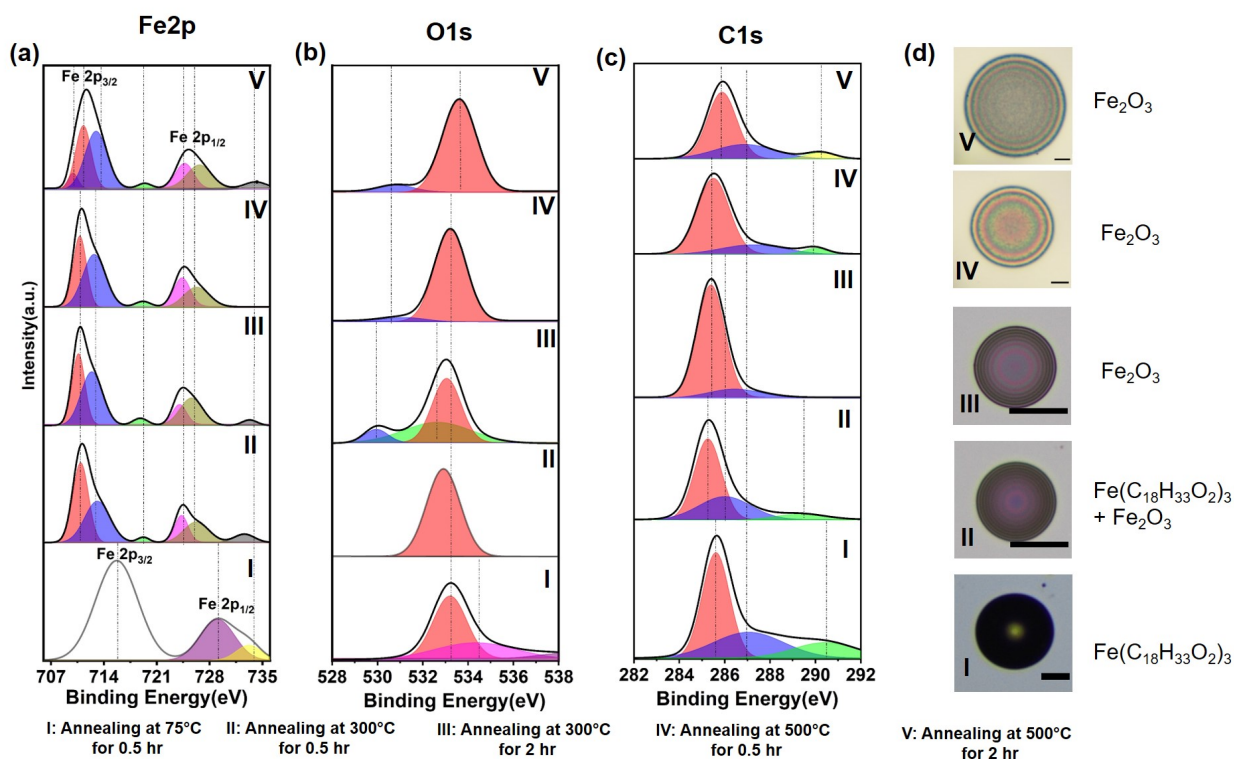


**Figure 4.** XPS spectra of the surface droplets after various heating process. (a) Iron  $Fe2p$  spectra (b) Oxygen  $O1s$  spectra (c) Carbon  $C1s$  spectra. Black solid line is cumulative observed values of binding energy for each element. Filled area under different colours denotes deconvoluted peaks during peak fittings. (d) Optical images of nanocaps after different heating process. Treatment conditions I-V are listed in Table 1. Length of scale bar: 15  $\mu m$ .

Figure 4 shows the XPS spectra of oleate droplets and nanocaps treated at different heating temperatures and times. Iron oleate remains in the liquid state until 80°C without decomposition.<sup>50–52</sup> The peaks of Fe 2p, O 1s and C 1s listed in Table 2 and 3 are compared to distinguish the chemical states of the products.

The deconvolution of  $Fe2p$  spectra resolves the peaks at 715.6 eV, 726.6 eV and 734.3 eV due to the presence of  $Fe^{3+}$  states within the iron oleate complex. The presence of  $Fe^{3+}$  in the complexes is attributed to the reaction between  $FeCl_3$  and the droplets of oleic acid.<sup>36,53</sup>

**Table 2.** XPS peaks of Fe2p

Peak location(eV)	Indicated component	Treatment conditions
715.6	$Fe^{3+}2p_{3/2}$ <sup>42</sup>	I
726.6	$Fe^{3+}2p_{1/2}$ <sup>43</sup>	I
734.3	$Fe^{3+}2p_{1/2}$ satellite <sup>43</sup>	I-V
710.9, 713.2	$Fe^{3+}$ octahedral <sup>44</sup>	II, III
724.5	$Fe^{3+}2p_{1/2}$ in $Fe_2O_3$ <sup>44</sup>	II-V
709.9, 711.3, 713.0	$\alpha - Fe_2O_3$ <sup>42</sup>	IV, V
719	$Fe_2O_3$ <sup>44,45</sup>	II-V

**Table 3.** XPS peaks of O1s and C1s

Peak location(eV)	Indicated component	Treatment conditions
533.3-533.8	$SiO_2$ <sup>46</sup>	I-V
530.8	Oxide species <sup>47</sup>	IV, V
285.1	Alkyl chains <sup>44</sup>	I, II
287.0	C-O bound <sup>48</sup>	I, II
290.5	C (carboxyl) <sup>49</sup>	I

The binding energy of oxygen for  $O1s$  at the peak of 533.3 eV is assigned to  $SiO_2$  of the substrate.<sup>46</sup> XPS peak for carbon ( $C1s$ ) at  $\sim 285.1$  eV indicates the existence of alkyl chain in oleate,<sup>44</sup> while the peak of 287.0 eV is attributed to C-O bond<sup>48</sup> from the oleate. The peak at 290.5 eV is assigned to carboxyl carbon in organic acid.<sup>49</sup> Single carbon-oxygen (C-O) and carboxyl carbon are present in both oleic acid and iron oleate complex.

As the heating temperature increased to 300°C at 0.5 hr and 2 hr, iron oleate droplets solidified as shown in Figure 4d-II and III. XPS analysis of heated droplets at 300 °C shows that presence of  $Fe_2O_3$  instead of  $Fe_3O_4$ .<sup>44,45</sup> The peaks of 285.1 eV and 287.0 eV, as explained above, originate from the iron oleate, possibly due to the incomplete decomposition of the iron oleate during heating to 300°C at both 0.5hr and 2 hr.<sup>36,54</sup>

The XPS analysis above suggests that the decomposition of iron oleate started at 300 °C.



when the heating temperature increased to 500 ° at 0.5 hr and 2 hr, we observed the formation of iron oxide ( $\alpha - Fe_2O_3$ ) phase nanocaps after 2 hr, as shown in Figure 4d-IV and V. XPS

analysis of the heated substrate at 500° for 2 hr confirms the appearance of  $\alpha - Fe_2O_3$  phase. Here the analysis of XPS spectra shows that heating at 500°C provides sufficient temperature for the formation of iron oxide from the iron oleate complex. The formation of the  $\alpha - Fe_2O_3$  can be further confirmed by TEM and simulation.

To further confirm the formation of  $\alpha - Fe_2O_3$  after heating at 500°C for 2 hr. TEM and

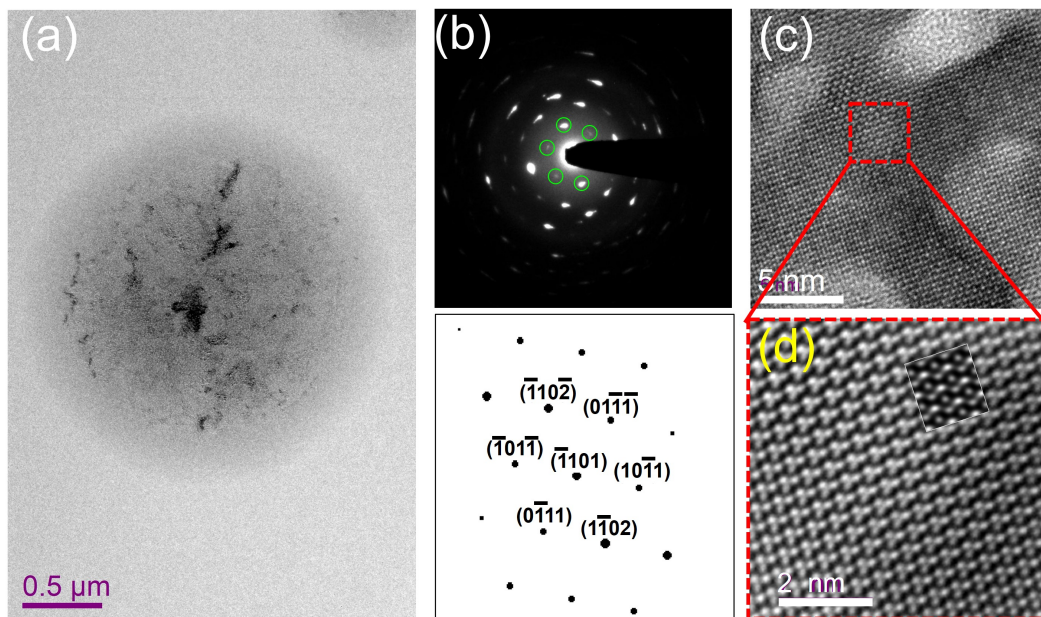


**Figure 5.** (a) TEM images of nanocaps heated at 500° for 2 hrs. (b) The corresponding selected-area electron beam diffraction (SAED) pattern image together with its simulation. (c) The high-resolution TEM (HRTEM) image of (a). (d) HRTEM of a higher magnification for the area indicated by a square in (c) and the simulation of the HRTEM image illustrated by a rectangle inset with white profile.

its simulation were used. Regions with deep contrast are emerged in the nanocap, as shown in Figure 5a. The corresponding SAED exhibits a spot-like feature of the typical crystalline phase, as shown in Figure 5b. The simulation of the SAED pattern in Figure 5b suggests that  $\alpha - Fe_2O_3$  formed. The reflection spots circled are related corresponding to the labeled dots in the SAED simulating pattern. Close check the diffraction pattern finds that instead of a sharp, well-defined circular shape, the reflection spots are stretched into the curved shape. This depicts the formed  $\alpha - Fe_2O_3$  possesses a certain extent of texture.

Usually, the driving force for crystallization is mainly due to dislocation, grain boundary

energy, surface energy and strain energy or their combinations. During the crystallization process, a texture structure can form. It is well known that surface energy plays an important role in the formation of texture structures. In the study of Stirner et al about the surface energy of  $\alpha\text{-Fe}_2\text{O}_3$ ,<sup>55</sup> they found that the surface energy decreased in a sequence of  $\{01\bar{1}2\} < \{0001\} < \{11\bar{2}0\} < \{10\bar{1}0\} \approx \{10\bar{1}1\} < \{11\bar{2}6\} < \{10\bar{1}2\}$ . The  $\{10\bar{1}1\}$  shown in the current study (see Figure 5b) is at a position of high surface energy in the sequence. We postulate that the surface energy does not play the main role in the texture formation mechanism; rather, strain energy has more impact on the texture structure arrangement.

The high resolution TEM (HRTEM) image indicates that  $\alpha\text{-Fe}_2\text{O}_3$  possesses a well-defined crystal structure (Figure 5c). This suggests that crystalline  $\alpha\text{-Fe}_2\text{O}_3$  has already formed before 500°C. Heating at 500°C for 2 hr gives  $\alpha\text{-Fe}_2\text{O}_3$  enough energy and time to grow into a complete structure. Because dislocation is an important reason for the formation of texture structure, the rare existence of dislocation in the TEM observation for  $\alpha\text{-Fe}_2\text{O}_3$  treated at 500°C indicates that a well-defined crystal structure does form. As shown in Figure 5d, the simulated HRTEM image is overlapped with the experimental one. It is seen that they match very well. This is, from an alternative way, to confirm the formation of 500°C phase.

Hematite nanocrystals ( $\alpha\text{-Fe}_2\text{O}_3$ ) were synthesized previously using oleic acid as precursor solution or surfactant.<sup>56</sup> The development of crystalline phase of  $\alpha\text{-Fe}_2\text{O}_3$  for iron oxide material was largely synthesized by using various conditions such as time-dependent (1-72 hr), different temperature ranges and change in precursors.<sup>30,57</sup> Here, we coined a simple, straight and facile approach to develop  $\alpha\text{-Fe}_2\text{O}_3$  phase via solvent approach without using any post surfactant and precursor solution modification.

## Formation of porous nanocaps from binary surface nanodroplets

The morphology and structure of the nanocaps can be modulated by doping nonreactive liquid in nanodroplets. As shown in Figure 6a and b, when the droplets consist of a mixture

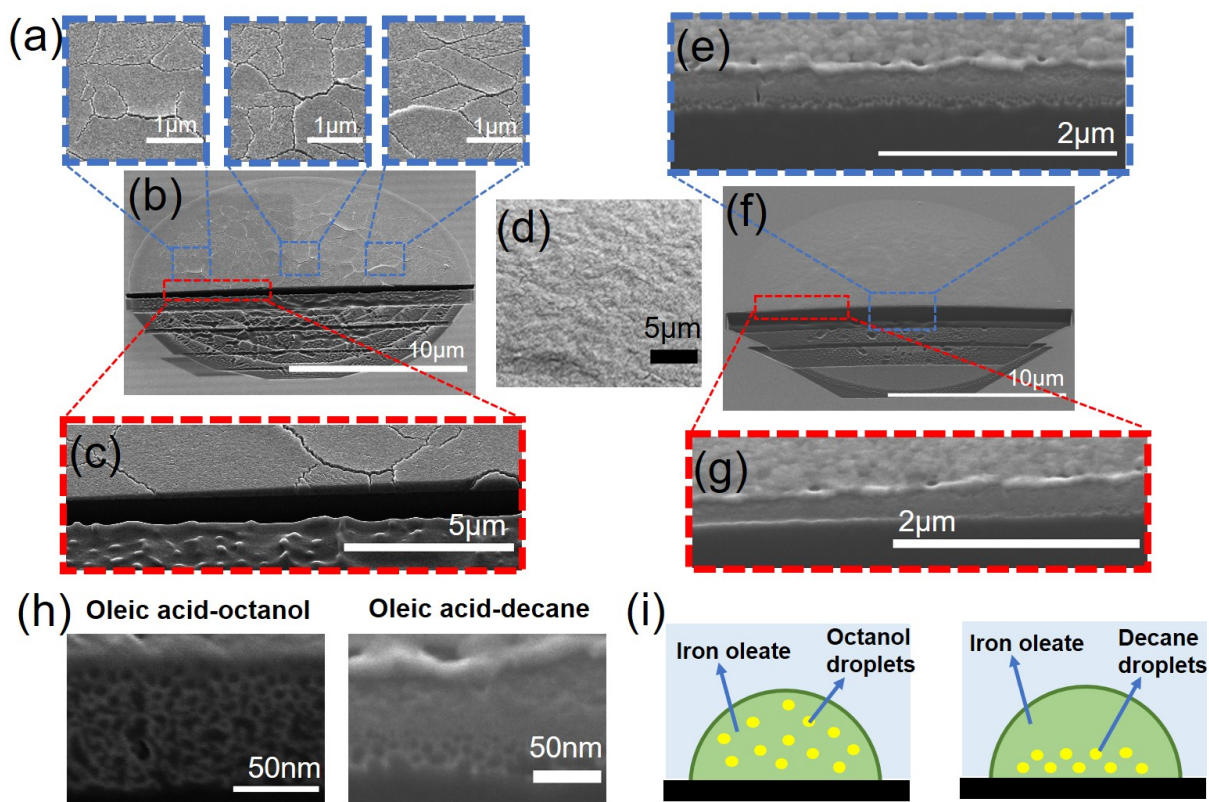


**Figure 6.** Surface and inner structures of iron oxide nanocaps fabricated from binary surface nanodroplets. (a) shows the creviced surface of the nanocap from oleic acid-octanol binary surface droplets. (b) The FIB-milled nanocap was fabricated from oleic acid-octanol binary surface droplets. (c) shows the inner structure of (b), indicating that the height of the nanocap increases toward to the center. (d) The rough but uncracked surface of the nanocap from pure oleic acid droplets. (e) and (g) show the inner structure of the nanocap synthesized from oleic acid-decane binary surface droplets (f), similar to the shape of (c). (h) High resolution images of the porous structure of the nanocaps synthesized from oleic acid-octanol binary surface droplets and oleic acid-decane binary surface droplets, respectively. (i) The sketch of the reaction process of binary surface nanodroplets with iron precursor.

of oleic acid and octanol, the produced nanocaps exhibit many crevices on the surface. In contrast, the surface of the nanocaps synthesized from pure oleic acid shows a rough but uncracked surface, as shown in Figure 6d. Those crevices on the nanocaps are around 40 nm in width. When the droplets are a mixture of oleic acid and decane, the structure that are synthesized from binary droplets of oleic acid-decane also have the shape of a thin and solidified spherical cap with a similar aspect ratio as the nanocaps from a single droplet, as shown in Figure 6(e-g).

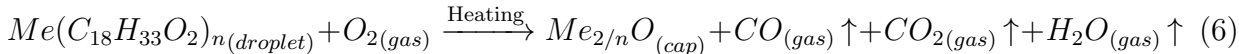
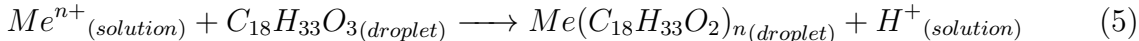
A distinct feature of the nanocaps formed from binary droplets of oleic acid and octanol is the highly porous inner structure, as shown in Figure 6h. In contrast, the nanocaps synthesized from the binary droplets of oleic acid and decane are more porous in the segment near the supporting substrate (Figure 6h).

It is interesting why the porous inner structure of nanocaps is formed from binary droplets. Based on the ratio of oleic acid and the solubility diagram in Figure 1c and d, the binary droplets mainly consist of oleic acid.<sup>21</sup> The appearance of the porous inner structure of nanocaps is most likely caused by the formation of the daughter droplets from the nonreactive liquid (1-octanol and decane) inside the droplets as well as the produced liquid from the reaction of oleic acid and iron precursor. The secondary oil small droplets may template the porous inner structure of the final nanocaps.

There is a difference in the surface activity of octanol and decane. Octanol is amphiphilic similar to oleic acid, while the later molecules are non-polar. Thus, during the reaction with the iron precursor, decane may reside inside the droplets. As oleic acid is converted to oleate, decane is pushed away from the droplet surface. As decane is oversaturated, forming daughter droplets located near the substrate base, as sketched in Figure 6i. In contrast, octanol uniformly distributes in the droplet due to its amphiphilic property. During heating, octanol or decane droplets evaporates, leading to permanent pores inside of the nanocaps.

## Formation of other metal oxide nanocaps

The droplets of oleic acid are able to react with many metal precursors; hence the surface nanodroplet template method is effective for the synthesis of a wide range of metal oxide nanocaps. As a demonstration, we have expanded the approach for the synthesis of copper oxide, yttrium oxide and zinc oxide nanocap on the substrate, as shown in Figure 7. The reaction for the formation of metal oleates and the subsequential thermal decomposition process is shown below.



Here,  $Me$  represents metal elements. The mass loss in the production of  $CuO$ ,  $Y_2O_3$  and  $ZnO$  from the thermal decomposition is estimated to be 87.3%, 87.6% and 87.0% , respectively, leading to a significant reduction in surface coverage compared to that of initial droplets. Optical microscope images show that yttrium oxide nanocaps are yellow in the center and blue around the rim, while zinc oxide nanocaps show a light blue color all over the caps, as shown in Figure 7b and c. As for copper oxide, the optical image shows a dark and imperfectly spherical cap shape, as shown in Figure 7a. The color difference in nanocaps of copper oxide, yttrium oxide and zinc oxide and iron oxide may be attributed to the refractive index of these two metal oxides. SEM images in Figure 7 show that the morphology of yttrium oxide is similar to iron oxide with a smooth surface. In contrast, copper oxide has a rough surface caused by the aggregation of the copper oxide nanoparticles. While zinc oxide shows a close texture of aggregation of non-spherical nanoparticles.

The successful synthesis of nanocaps of copper oxide, yttrium oxide and zinc oxide demonstrates that our method is general for forming diverse metal oxide nano/microstructures on a substrate. The universality of this method has the potential for developing surface-bound nanomaterials in many areas, including plasmonic effect, photo-illumination enhancement,

catalytic reaction and among others.

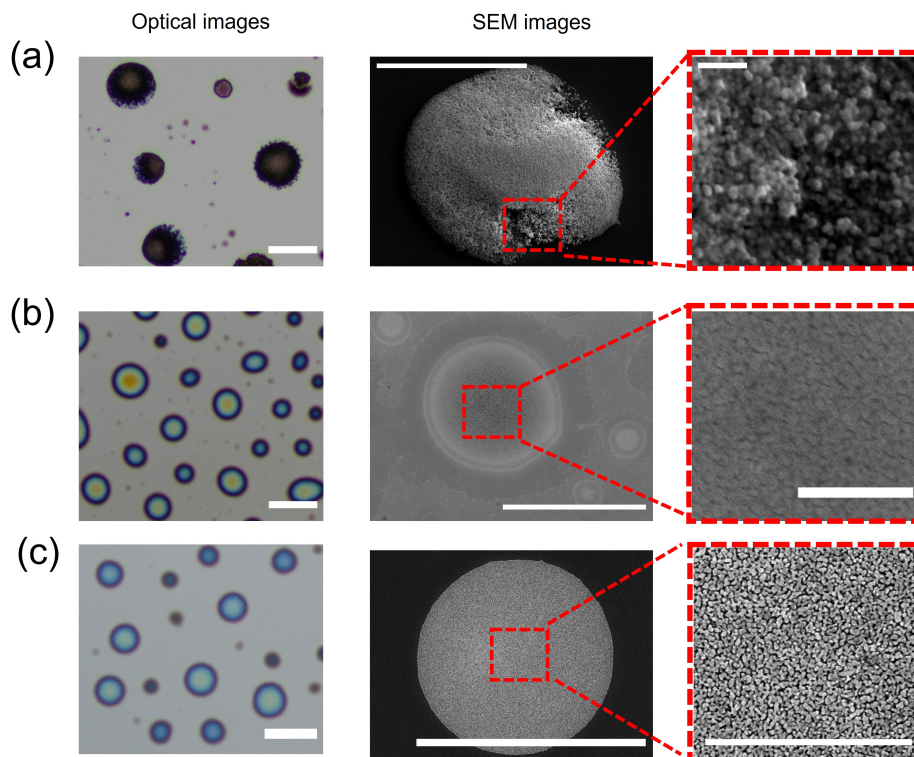


**Figure 7.** Optical (first column) and SEM images (second and third columns) of nanocaps of copper oxide (a), yttrium oxide (b) and Zinc oxide (c). Length of scale bare:  $25 \mu m$  (first column),  $15 \mu m$  (second column) and  $2 \mu m$  (third column).

The as-produced nanocaps show strong adhesion to the substrate. The stability of the surface-bound nanocaps of iron oxide has been tested by sonication. After sonication for 60 minutes, the small nanocaps remained intact on the surface (SI-5a), while some of the large nanocaps were removed from the substrate. The surface coverage reduction by sonication treatment is more obvious for large nanocaps than for small nanocaps (SI-5c).

We attribute the particularly strong adhesion between the caps and the substrate to the intimate contact between the iron oxide and the supporting substrate formed during the in-situ fabrication process and their strong van der Waal's interaction.<sup>58</sup> Small nanocaps are even more resilient to sonication due to less probability of colliding the cavitation bubbles.

## Porous nanocaps for photodegradation

Nanocaps prepared in this work have the direct application potential for photocatalytic reactions in a flow-in chamber, demonstrated by photodegradation of methyl orange (MO) in the flow. As a demonstration, the iron oxide nanocaps of three different porosities were fabricated on a hydrophobized glass substrate and then was heated at 500 °C in air for 2 hours. The products have been proven to be  $\alpha - Fe_2O_3$  from the characterization in Figure 4. Nanocap (1) was prepared from pure oleic acid droplets. Nanocap (2) was from oleic acid-decane binary droplets and Nanocap (3) was from oleic acid-octanol binary droplets. As shown in Figure 8b and c, the surface coverage of those three nanocaps are 25%, 22% and 10%, respectively. The relative low photodegradation efficiency from the low surface coverage allowed us to identify the enhancement from porous structures.

The photo-catalytical reaction was performed in a micro-fluid chamber under visible light. The model compound was a dye (MO). As shown in Figure 8a, the nanocaps of iron oxide on the top glass plate headed down to the inner chamber as the dye solution flow through before being collected into a vial from the outlet.

The spectra of the UV-vis of the dye solution show a peak of absorbance around 464 nm. The efficiency of the degradation was evaluated by the intensity of the peak, as shown in Supporting information SI-6. The existence of the iron oxide nanocap can improve the efficiency at least more than 7 times of the bare glass slide. The improvement in degradation efficiency is attributed to the catalytic activity of iron oxide nanocaps. As shown in Figure 2c, 4b and 8a, the as-prepared nanocaps are ultra-thin and semitransparent. The light can pass the nanocaps into the solution phase. Herein, they are suitable for photocatalytic reactions.

The nanocaps with porous structures have obviously higher degradation efficiency. In Figure 8, the degradation efficiencies from three porosities are normalized by the surface coverage of the nanocaps. The normal efficiency for the most porous Nanocaps (No. 3) is more than twice of the efficiency for smooth nanocaps (No. 1). Nanocaps (1) without pores are the least

effective for photodegradation. Clearly, the porous structure enhances the photodegradation due to the more surface area available for catalysis. The degradation efficiency may be further improved by optimizing the exposure time and, more effectively, by increasing the surface coverage of iron oxide nanocaps.

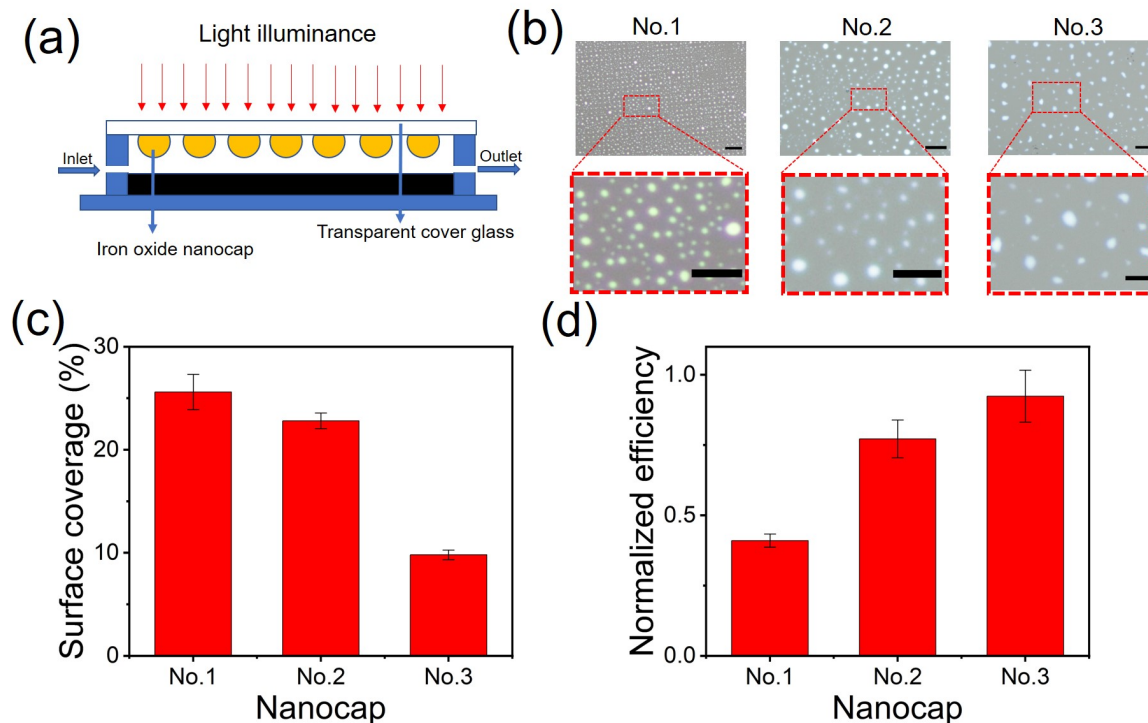


**Figure 8.** (a) Sketch of the fluid chamber for photo-degradation test. (b) Optical images of non-porous nanocaps (No.1), moderately porous nanocaps (No.2) and highly porous nanocaps (No.3) on the glass slide. (c) The surface coverage of the nanocaps corresponding to (b). (d) Normalized efficiency of photodegradation by nanocaps. The efficiencies are normalized by dividing the net efficiency of  $(E_{cap}-E_{glass})$  by surface coverage (S). Length of scale bar in (b):  $25 \mu m$  (top row) and  $15 \mu m$  (bottom row).

## Conclusions

In conclusion, we demonstrate an approach based on reactive surface nanodroplets for in-situ fabrication of metal oxide nanocaps with the controlled spatial arrangement and surface coverage on a solid surface. The crystalline structure of nanocaps can be conveniently varied in the post synthesis process of the droplet reaction via thermal treatment. Notably, nanocaps

with nanoporous structures can be produced by doping nonreactive liquid in reactive surface droplets. As applied to catalyze photodegradation of organic compounds in water, the porous nanocaps exhibit better performance as compared to smooth nanocaps. Reactive surface nanodroplets may open the window to the in-situ synthesis of a range of surface-bound nanomaterials applied in the catalytic reaction, optical focusing and solar energy conversion.

## Acknowledge

The project is supported by the Natural Science and Engineering Research Council of Canada (NSERC), Future Energy Systems (Canada First Research Excellence Fund) and NRC-Nanotechnology Research Center (NRC-NANO). The second author Tulsi Satyavir Dabodiya would like to thank the Science and Engineering Research Board (SERB), Department of Science and Technology, Government of India for facilitating the overseas visiting doctoral fellowship (OVDF).

## References

- (1) Raza, A.; Alketbi, A. S.; Devarapalli, R.; Li, H.; Zhang, T. Refractory Ultrathin Nanocomposite Solar Absorber with Superior Spectral Selectivity and Thermal Stability. *Adv. Opt. Mater.* **2020**, *8*, 2000679.
- (2) Wang, Y.; Wu, X.; Shao, B.; Yang, X.; Owens, G.; Xu, H. Boosting solar steam generation by structure enhanced energy management. *Sci. Bull.* **2020**, *65*, 1380–1388.
- (3) Lu, Y.; Fan, D.; Xu, H.; Min, H.; Lu, C.; Lin, Z.; Yang, X. Implementing hybrid energy harvesting in 3D spherical evaporator for solar steam generation and synergic water purification. *Sol. RRL* **2020**, *4*, 2000232.
- (4) Li, R.; Shi, Y.; Wu, M.; Hong, S.; Wang, P. Photovoltaic panel cooling by atmospheric water sorption–evaporation cycle. *Nat. Sustain* **2020**, *3*, 636–643.

- (5) García-Muñoz, P.; Fresno, F.; Lefevre, C.; Robert, D.; Keller, N. Ti-Modified LaFeO<sub>3</sub>/β-SiC Alveolar Foams as Immobilized Dual Catalysts with Combined Photo-Fenton and Photocatalytic Activity. *ACS Appl. Mater. Interfaces* **2020**, *12*, 57025–57037.
- (6) Stergiou, A.; Tagmatarchis, N. Fluorene–perylene diimide arrays onto graphene sheets for photocatalysis. *ACS Appl. Mater. Interfaces* **2016**, *8*, 21576–21584.
- (7) Fan, G.; Ning, R.; Li, X.; Lin, X.; Du, B.; Luo, J.; Zhang, X. Mussel-Inspired Immobilization of Photocatalysts with Synergistic Photocatalytic–Photothermal Performance for Water Remediation. *ACS Appl. Mater. Interfaces* **2021**,
- (8) Bailey, D. C.; Langer, S. H. Immobilized transition-metal carbonyls and related catalysts. *Chem. Rev.* **1981**, *81*, 109–148.
- (9) Wei, Z.; Li, Y.; Cooks, R. G.; Yan, X. Accelerated reaction kinetics in microdroplets: overview and recent developments. *Annu. Rev. Phys. Chem.* **2020**, *71*, 31–51.
- (10) Fallah-Araghi, A.; Meguellati, K.; Baret, J.-C.; El Harrak, A.; Mangeat, T.; Karplus, M.; Ladame, S.; Marques, C. M.; Griffiths, A. D. Enhanced chemical synthesis at soft interfaces: A universal reaction-adsorption mechanism in microcompartments. *Phys. Rev. Lett.* **2014**, *112*, 028301.
- (11) Han, X.; Koh, C. S. L.; Lee, H. K.; Chew, W. S.; Ling, X. Y. Microchemical plant in a liquid droplet: plasmonic liquid marble for sequential reactions and attomole detection of toxin at microliter scale. *ACS Appl. Mater. Interfaces* **2017**, *9*, 39635–39640.
- (12) Li, Z.; Kiyama, A.; Zeng, H.; Lohse, D.; Zhang, X. Speeding up biphasic reactions with surface nanodroplets. *Lab Chip* **2020**, *20*, 2965–2974.
- (13) Zhang, X.; Wei, Z.; Choi, H.; Hao, H.; Yang, H. Oiling-Out Crystallization of Beta-

- Alanine on Solid Surfaces Controlled by Solvent Exchange. *Adv. Mater. Interfaces* **2021**, *8*, 2001200.
- (14) Dyett, B. P.; Zhang, X. Accelerated Formation of H<sub>2</sub> Nanobubbles from a Surface Nanodroplet Reaction. *ACS nano* **2020**, *14*, 10944–10953.
- (15) Zhu, Q.-L.; Xu, Q. Immobilization of ultrafine metal nanoparticles to high-surface-area materials and their catalytic applications. *Chem* **2016**, *1*, 220–245.
- (16) Rebrov, E. V.; Klinger, E. A.; Berenguer-Murcia, A.; Sulman, E. M.; Schouten, J. C. Selective hydrogenation of 2-methyl-3-butyne-2-ol in a wall-coated capillary microreactor with a Pd<sub>25</sub>Zn<sub>75</sub>/TiO<sub>2</sub> catalyst. *Org. Process Res. Dev.* **2009**, *13*, 991–998.
- (17) Zhang, L.; Liu, Z.; Wang, Y.; Xie, R.; Ju, X.-J.; Wang, W.; Lin, L.-G.; Chu, L.-Y. Facile immobilization of Ag nanoparticles on microchannel walls in microreactors for catalytic applications. *Chem. Eng. J* **2017**, *309*, 691–699.
- (18) Merckle, C.; Blümel, J. Improved rhodium hydrogenation catalysts immobilized on oxidic supports. *Adv. Synth. Catal.* **2003**, *345*, 584–588.
- (19) Zhang, X.; Lu, Z.; Tan, H.; Bao, L.; He, Y.; Sun, C.; Lohse, D. Formation of surface nanodroplets under controlled flow conditions. *Proc. Natl. Acad. Sci. U. S. A.* **2015**, *112*, 9253–9257.
- (20) Gregson, F.; Robinson, J.; Miles, R.; Royall, C.; Reid, J. Drying kinetics of salt solution droplets: Water evaporation rates and crystallization. *J. Phys. Chem. B* **2018**, *123*, 266–276.
- (21) Li, M.; Bao, L.; Yu, H.; Zhang, X. Formation of multicomponent surface nanodroplets by solvent exchange. *J. Phys. Chem. C* **2018**, *122*, 8647–8654.
- (22) Abianeh, O. S.; Chen, C.-P.; Mahalingam, S. Numerical modeling of multi-component fuel spray evaporation process. *Int. J. Heat Mass Transfer* **2014**, *69*, 44–53.

- (23) Shakiba, S.; Mansouri, S.; Selomulya, C.; Woo, M. The role of the intermediate stage of drying on particle in-situ crystallization in spray dryers. *Powder Technol.* **2018**, *323*, 357–366.
- (24) Tan, H.; Diddens, C.; Lv, P.; Kuerten, J. G.; Zhang, X.; Lohse, D. Evaporation-triggered microdroplet nucleation and the four life phases of an evaporating Ouzo drop. *Proc. Natl. Acad. Sci. U. S. A.* **2016**, *113*, 8642–8647.
- (25) Yu, H.; Peng, S.; Lei, L.; Zhang, J.; Greaves, T. L.; Zhang, X. Large Scale Flow-Mediated Formation and Potential Applications of Surface Nanodroplets. *ACS Appl. Mater. Interfaces* **2016**, *8*, 22679–22687.
- (26) Yu, H.; Rump, M.; Maheshwari, S.; Bao, L.; Zhang, X. Growth of nanodroplets on a still microfiber under flow conditions. *Phys. Chem. Chem. Phys.* **2018**, *20*, 18252–18261.
- (27) Bao, L.; Pinchasik, B.-E.; Lei, L.; Xu, Q.; Hao, H.; Wang, X.; Zhang, X. Control of Femtoliter Liquid on a Microlens: A Way to Flexible Dual-Microlens Arrays. *ACS Appl. Mater. Interfaces* **2019**, *11*, 27386–27393.
- (28) Li, M.; Dyett, B.; Yu, H.; Bansal, V.; Zhang, X. Functional femtoliter droplets for ultra-fast nanoextraction and supersensitive online microanalysis. *Small* **2019**, *15*, 1804683.
- (29) Xu, P.; Zeng, G. M.; Huang, D. L.; Feng, C. L.; Hu, S.; Zhao, M. H.; Lai, C.; Wei, Z.; Huang, C.; Xie, G. X., et al. Use of iron oxide nanomaterials in wastewater treatment: a review. *Sci. Total Environ.* **2012**, *424*, 1–10.
- (30) Mishra, M.; Chun, D.-M.  $\alpha$ -Fe<sub>2</sub>O<sub>3</sub> as a photocatalytic material: A review. *Appl. Catal., A* **2015**, *498*, 126–141.
- (31) Khedr, M.; Halim, K. A.; Soliman, N. Synthesis and photocatalytic activity of nano-sized iron oxides. *Mater. Lett.* **2009**, *63*, 598–601.

- (32) Ge, S.; Shi, X.; Sun, K.; Li, C.; Uher, C.; Baker Jr, J. R.; Banaszak Holl, M. M.; Orr, B. G. Facile hydrothermal synthesis of iron oxide nanoparticles with tunable magnetic properties. *J. Phys. Chem. C* **2009**, *113*, 13593–13599.
- (33) Li, S.; Zhang, T.; Tang, R.; Qiu, H.; Wang, C.; Zhou, Z. Solvothermal synthesis and characterization of monodisperse superparamagnetic iron oxide nanoparticles. *J. Magn. Mater.* **2015**, *379*, 226–231.
- (34) Lassoued, A.; Lassoued, M. S.; Dkhil, B.; Gadri, A.; Ammar, S. Structural, optical and morphological characterization of Cu-doped  $\alpha$ -Fe<sub>2</sub>O<sub>3</sub> nanoparticles synthesized through co-precipitation technique. *J. Mol. Struct.* **2017**, *1148*, 276–281.
- (35) Gao, C.; Lyu, F.; Yin, Y. Encapsulated metal nanoparticles for catalysis. *Chem. Rev.* **2020**,
- (36) Bronstein, L. M.; Huang, X.; Retrum, J.; Schmucker, A.; Pink, M.; Stein, B. D.; Dragnea, B. Influence of iron oleate complex structure on iron oxide nanoparticle formation. *Chem. Mater.* **2007**, *19*, 3624–3632.
- (37) Hufschmid, R.; Arami, H.; Ferguson, R. M.; Gonzales, M.; Teeman, E.; Brush, L. N.; Browning, N. D.; Krishnan, K. M. Synthesis of phase-pure and monodisperse iron oxide nanoparticles by thermal decomposition. *Nanoscale* **2015**, *7*, 11142–11154.
- (38) Chen, Z. Size and shape controllable synthesis of monodisperse iron oxide nanoparticles by thermal decomposition of iron oleate complex. *Synth. React. Inorg., Met.-Org., Nano-Met. Chem.* **2012**, *42*, 1040–1046.
- (39) Koga, N.; Sato, Y. Formation and transformation kinetics of amorphous iron (III) oxide during the thermally induced transformation of ferrous oxalate dihydrate in air. *J. Phys. Chem. A* **2011**, *115*, 141–151.

- (40) Zhang, X.; Ren, J.; Yang, H.; He, Y.; Tan, J.; Qiao, G. G. From transient nanodroplets to permanent nanolenses. *Soft Matter* **2012**, *8*, 4314–4317.
- (41) Lohse, D.; Zhang, X. Physicochemical hydrodynamics of droplets out of equilibrium. *Nat. Rev. Phys.* **2020**, *2*, 426–443.
- (42) Grosvenor, A.; Kobe, B.; Biesinger, M.; McIntyre, N. Investigation of multiplet splitting of Fe 2p XPS spectra and bonding in iron compounds. *Surf. Interface Anal.* **2004**, *36*, 1564–1574.
- (43) Mann, J.; Doluda, V. Y.; Leonard, C.; Losovyj, Y. B.; Morgan, D. G.; Bukalov, S. S.; Shifrina, Z.; Stein, B. D.; Cherkasov, N.; Rebrov, E. V., et al. Metal oxide–zeolite composites in transformation of methanol to hydrocarbons: do iron oxide and nickel oxide matter? *RSC Adv.* **2016**, *6*, 75166–75177.
- (44) Wilson, D.; Langell, M. XPS analysis of oleylamine/oleic acid capped Fe<sub>3</sub>O<sub>4</sub> nanoparticles as a function of temperature. *Appl. Surf. Sci.* **2014**, *303*, 6–13.
- (45) Yamashita, T.; Hayes, P. Analysis of XPS spectra of Fe<sup>2+</sup> and Fe<sup>3+</sup> ions in oxide materials. *Appl. Surf. Sci.* **2008**, *254*, 2441–2449.
- (46) Jensen, D. S.; Kanyal, S. S.; Madaan, N.; Vail, M. A.; Dadson, A. E.; Engelhard, M. H.; Linford, M. R. Silicon (100)/SiO<sub>2</sub> by XPS. *Surf. Sci. Spectra* **2013**, *20*, 36–42.
- (47) Sayyed, B.; Chatterjee, A.; Kanetkar, S.; Badrinarayanan, S.; Date, S. Surface characterisation of an iron oxide catalyst (ethylbenzene→ styrene): An xps study. *Proc. Indian Acad. Sci.* 1985; pp 291–295.
- (48) Ch'Ng, Y.; Loh, K.; Daud, W.; Mohamad, A. Synthesis and characterization of sulfonated graphene oxide nanofiller for polymer electrolyte membrane. *IOP Conf. Ser.: Mater. Sci. Eng.* 2016; p 012035.

- (49) Peng, X.; Barteau, M. Spectroscopic characterization of surface species derived from  $HCOOH$ ,  $CH_3COOH$ ,  $CH_3OH$ ,  $C_2H_5OH$ ,  $HCOOCH_3$ , and  $C_2H_2$  on MgO thin film surfaces. *Surf. Sci.* **1989**, *224*, 327–347.
- (50) Ullrich, A.; Rahman, M. M.; Longo, P.; Horn, S. Synthesis and high-resolution structural and chemical analysis of iron-manganese-oxide core-shell nanocubes. *Sci. Rep.* **2019**, *9*, 1–9.
- (51) Lin, M. M.; Kim, D. K. In situ thermolysis of magnetic nanoparticles using non-hydrated iron oleate complex. *J. Nanopart. Res.* **2012**, *14*, 1–13.
- (52) Roonasi, P.; Holmgren, A. A Fourier transform infrared (FTIR) and thermogravimetric analysis (TGA) study of oleate adsorbed on magnetite nano-particle surface. *Appl. Surf. Sci.* **2009**, *255*, 5891–5895.
- (53) Nakamoto, T.; Hanaya, M.; Katada, M.; Endo, K.; Kitagawa, S.; Sano, H. The Valence-Detrapping Phase Transition in a Crystal of the Mixed-Valence Trinuclear Iron Cyanoacetate Complex  $[Fe_3O(O_2CCH_2CN)_6(H_2O)_3]$ . *Inorg. Chem.* **1997**, *36*, 4347–4359.
- (54) Chang, K.-C.; Ji, W.-F.; Lai, M.-C.; Hsiao, Y.-R.; Hsu, C.-H.; Chuang, T.-L.; Wei, Y.; Yeh, J.-M.; Liu, W.-R. Synergistic effects of hydrophobicity and gas barrier properties on the anticorrosion property of PMMA nanocomposite coatings embedded with graphene nanosheets. *Polym. Chem.* **2013**, *5*, 1049–1056.
- (55) Stirner, T.; Scholz, D.; Sun, J. Ab initio simulation of structure and surface energy of low-index surfaces of stoichiometric  $\alpha$ -Fe<sub>2</sub>O<sub>3</sub>. *Surf. Sci.* **2018**, *671*, 11–16.
- (56) Wang, S.-B.; Min, Y.-L.; Yu, S.-H. Synthesis and magnetic properties of uniform hematite nanocubes. *J. Phys. Chem. C* **2007**, *111*, 3551–3554.

- (57) Meijer, J.-M.; Rossi, L. Preparation, properties, and applications of magnetic hematite microparticles. *Soft Matter* **2021**,
- (58) Israelachvili, J. N. *Intermolecular and surface forces*; Academic press, 2015; pp 107–130.